SPRINGER SERIES ON CHEMICAL SENSORS AND BIOSENSORS

07

Series Editor G. Urban

Volume Editors M. Zourob · A. Lakhtakia

Optical Guided-wave Chemical and Biosensors I

Broadband Spectroelectrochemical Interrogation of Molecular Thin Films by Single-Mode Electro-Active Integrated Optical Waveguides

Sergio B. Mendes, S. Scott Saavedra, and Neal R. Armstrong

Abstract Electron transfer processes to/from monolayers or submonolayers of surface-confined molecules are at the core of several established or emerging sensor technologies. Spectroelectrochemical techniques to monitor these redox processes combine spectroscopic information with the normally monitored electrochemical parameters, such as changes in current or voltage, and can be much more sensitive to changes in optical properties coupled with electron transfer than electrochemical techniques alone. Spectroelectrochemical techniques based on absorbance measurements typically suffer from low sensitivity owing to the low concentrations of redox active species on the surface, and their low absorptivities. Electro-active, single-mode waveguide technologies, developed over the last decade, have provided more than adequate sensitivity to characterize electron transfer to surface-confined molecules where the coverage can be as low as a few percent of a monolayer. In this chapter, we review the major developments in combining electrochemical analysis with optical platforms that maximize optical sensitivity, through the development of electro-active integrated planar waveguides operating in the single-mode optical regime. We provide here a general overview of the theoretical formalisms associated with light propagation and absorbance measurements in integrated optical waveguides, and their electro-active counterparts. We also describe the major implementations of the technology, including the extension of the single-mode configuration into a broadband spectroscopic tool to facilitate the interrogation of the entire visible wavelength region during the redox event, and review some specific applications of these techniques, which demonstrate its sensitivity and broad utility.

S.B. Mendes (✉)
Department of Physics and Astronomy, University of Louisville, KY, USA
e-mail: sb.mendes@louisville.edu

S.S. Saavedra and N.R. Armstrong
Department of Chemistry, University of Arizona, AZ, USA

M. Zourob and A. Lakhtakia (eds.), *Optical Guided-wave Chemical and Biosensors I*, Springer Series on Chemical Sensors and Biosensors 7,
DOI 10.1007/978-3-540-88242-8_4,

Keywords Spectroelectrochemistry · Integrated optical waveguides · Electrochemistry · Optical absorbance

Contents

Abbreviations

ASE	Amplified spontaneous emission
ATR	Attenuated total reflectance
CCD	Charge coupled device
CV	Cyclic voltamogramm
Cyt c	Cytochrome c
EA	Electro-active
IOW	Integrated optical waveguide
ITO	Indium tin oxide
MB	Methylene blue
NA	Numerical aperture
S	Sensitivity
TE	Transverse electric
TM	Transverse magnetic

1 Introduction

The need to combine conventional electrochemical measurements of electron transfer (ET) with spectroscopic probes was recognized over 40 years ago [1, 2]. It was quickly realized that optical spectroscopies, first applied to the visible

wavelength region, could provide much needed information about the extent and rates of ET, without the complications which accompany the measurement of current or potential versus time, arising from the charging and discharging of the electrical solution double layer adjacent to an electrode surface. Kuwana and coworkers [1, 2] are widely given credit for the development of the first effective spectroelectrochemical methods of electroanalysis, first using transmission through a semi-transparent electrode (the first electrodes were typically glass-coated with 100–200-nm-thick, antimony-doped tin oxide films), and subsequently attenuated total reflectance (ATR) using the same electrodes, in a simple total internal reflection geometry that achieved about 5 to 10 reflections over a total length of several centimeters.

For all such spectroelectrochemical experiments in the visible regime of the electromagnetic spectrum, if at least one redox state is strongly colored, spectroelectrochemical methods can provide a unique probe of the progress of the ET reaction, and characterization of the chemical reactions accompanying the primary ET event. One can reconstruct the Faradaic electrochemical current/voltage response from the absorbance changes accompanying ET, without the current or voltage response due to charging/discharging of the electrochemical double layer (ion motion in the solution region adjacent to the electrode), which accompany all ET reactions at solid electrodes. For low concentrations of the molecule in question, this proves to be a real asset, since the Faradaic current may be nearly impossible to resolve above the charging/discharging background current, and the optical response is completely decoupled from the charging/discharging event. Furthermore, only redox processes that produce an optical change are detected; thus, oxidation/reduction of a chromophore can be selectively detected in the presence of other redox-active but transparent species. An additional feature of spectroelectrochemical interrogation is that it can be performed over a broad spectral bandwidth, which allows for structural characterization of surface-confined chromophores (e.g., dimerization of phthalocyanines is accompanied by a shift in their visible absorbance spectra).

Early on, it was well recognized that spectroelectrochemical spectroscopies could potentially be used to study ET processes of many different types of surface-confined redox active molecules, such as organic dyes and heme proteins. However, many of these molecular systems do not possess a suitable combination of high surface coverage and molar absorptivity, necessitating enhancements in the sensitivity of the spectroelectrochemical platform. The obvious first choice is to decrease the thickness of the ATR element; for example, increasing the number of internal reflections from 1–2 per cm to 10–100 per cm can be achieved by using a 150-μm thick glass coverslip in place of a several millimeter thick ATR element. However, it was eventually realized that moving to single-mode waveguide platforms, where the effective number of reflections could be increased to well over 1,000 per cm, would push the sensitivity of spectroelectrochemical techniques in the visible wavelength region to the point where even submonolayer surface coverages of redox active molecules, with quite low absorptivities, could be characterized.

As a result of the work summarized in this chapter, unprecedented spectroelectrochemical sensitivity is now available in the visible wavelength region using broadband, single-mode waveguide platforms overcoated with semi-transparent conductive oxide electrode layers [3–5]. For certain molecular systems, it is now possible to monitor ET events for surface coverages of just a few percent of a monolayer (~10^{-12} moles/cm^2). This work has spawned the development of broadband spectroelectrochemical sensor platforms, which can combine both electrochemical signals (changes in potential or current versus time) and optical signals, to provide high sensitivities, and in some cases, unprecedented selectivity for multiple analytes whose redox activities are accompanied by spectral changes in distinct wavelength regions.

2 Optical Absorbance in Integrated Optical Waveguides

2.1 Single-Layer Waveguides

A basic waveguide structure, which is sketched in Fig. 1, is composed of a guiding layer surrounded by two semi-infinite media of lower refractive indices. The optical properties of the structure are described by the waveguiding layer refractive index n_w and thickness t, and by the refractive indices of the two surrounding semi-infinite media, here called n_c (for cover) and n_s (for substrate). Application of Maxwell's equations and boundary conditions leads to the well-known waveguide dispersion equation [6]:

$$\frac{2\pi t}{\lambda}\sqrt{{n_w}^2 - {N_{eff}}^2} = m\pi + \tan^{-1}\left[\left(\frac{n_w}{n_c}\right)^{2\rho}\sqrt{\frac{{N_{eff}}^2 - {n_c}^2}{{n_w}^2 - {N_{eff}}^2}}\right] + \tan^{-1}\left[\left(\frac{n_w}{n_s}\right)^{2\rho}\sqrt{\frac{{N_{eff}}^2 - {n_s}^2}{{n_w}^2 - {N_{eff}}^2}}\right], \quad (1)$$

where λ is the light wavelength in vacuum; N_{eff} is the effective refractive index of the waveguide; m is the order of the waveguide mode; $\rho = 0$ applies to transverse electric (TE) modes and $\rho = 1$ applies to transverse magnetic (TM) modes.

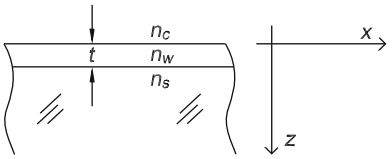

Fig. 1 A basic waveguide structure with a light-confining film of refractive index n_w and thickness t surrounded by two semi-infinite media of lower refractive indices: n_c and n_s

The waveguide effective refractive index, N_{eff}, of each guided mode, at a particular order and polarization, determines the phase velocity (c/N_{eff}) that a particular waveguide mode propagates along the waveguide surface. Its numerical value is typically calculated by solving the transcendental equation (1) using an iterative technique. Once the value of N_{eff} has been determined, then the field profile of that particular mode can be calculated. For instance, for the TE polarization, the electric field is described by [7]:

$$E_y(z) = E_c \exp\left[\frac{2\pi z}{\lambda}\sqrt{N_{\text{eff}}^2 - n_c^2}\right], \quad z \le 0 \tag{2}$$

$$E_y(z) = E_w \cos\left[\frac{2\pi z}{\lambda}\sqrt{n_w^2 - N_{\text{eff}}^2} - tan^{-1}\left(\frac{\sqrt{N_{\text{eff}}^2 - n_c^2}}{\sqrt{n_w^2 - N_{\text{eff}}^2}}\right)\right], \quad 0 \le z \le t, \tag{3}$$

$$E_y(z) = E_s \exp\left[-\frac{2\pi (z-t)}{\lambda}\sqrt{N_{\text{eff}}^2 - n_s^2}\right], \quad z \ge t, \tag{4}$$

with the following relation between the maximum field amplitudes in each region:

$$E_w\sqrt{n_w^2 - N_{\text{eff}}^2} = E_s\sqrt{n_w^2 - n_s^2} = E_c\sqrt{n_w^2 - n_c^2}. \tag{5}$$

As expected for a guided mode, the electric field in the substrate and cover regions decays exponentially, and it shows an oscillatory behavior inside the waveguide film. For the TM polarization, one obtains similar, although not identical, relations for the magnetic field H_y, which then allows the calculation of the Cartesian components E_x and E_z of the electric field using the generalized Ampere's law in the Maxwell's equations [7].

Absorbance calculations in the above configuration are implemented by introducing the absorbing species as a small perturbation to the initial configuration (see Fig. 2). Either a small extinction coefficient is introduced to the optical properties of the cover material (as shown in Fig. 3) or a thin absorbing layer is introduced between the waveguide and the cover (Fig. 4). A critical assumption for the

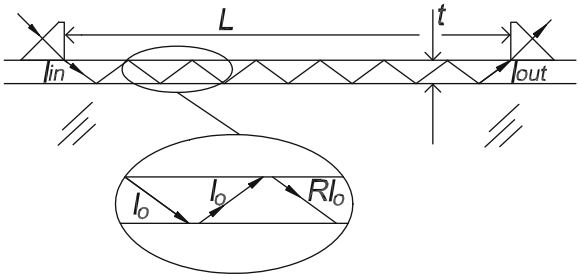

Fig. 2 Ray optics representation for absorbance calculations in a planar optical waveguide. Adapted from [8] with permission from the Optical Society of America, copyright 2000

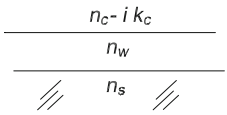

Fig. 3 Bulk solution absorption. Adapted from [8] with permission from the Optical Society of America, copyright 2000

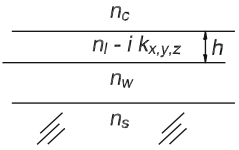

Fig. 4 Absorbance by a surface-adsorbed dichroic layer. Adapted from [8] with permission from the Optical Society of America, copyright 2000

absorbance calculations here is that the perturbation is small enough [8] so that N_{eff} of each mode can be used in the equations to follow. This assumption is valid to most relevant problems to be studied through waveguide modes and does not represent a serious limitation [8]. Under this assumption, the calculation of the attenuation coefficient, or absorbance, is straightforward. The introduction of an absorbing medium in proximity to the waveguide mode frustrates the total internal reflection at the waveguide-cover interface, as indicated at the upper interface in Fig. 2. The attenuation of the propagating guided mode can then be described by the reflectance, R, at the waveguide-cover interface. If we define η as the total number of reflections at the waveguide-cover interface, then the absorbance can be written as [8]:

$$A = -\log_{10}(R^{\eta}) \;\cong\; \frac{\eta\,(1-R)}{\ln(10)}, \tag{6}$$

where we have used the weak perturbation assumption ($R \cong 1$). The total number of reflections along the distance L between the input and output couplers is calculated from the ray optics model and given by:

$$\eta = \frac{\sqrt{n_{\text{w}}^2 - N_{\text{eff}}^2}}{2\,N_{\text{eff}}}\,\frac{L}{t_{\text{eff}}}. \tag{7}$$

The effective thickness, t_{eff}, takes into account the Goos-Hänchen shift effects and is given by:

$$t_{\text{eff,TE}} = t + \frac{\lambda/2\pi}{\sqrt{N_{\text{eff,TE}}^2 - n_{\text{c}}^2}} + \frac{\lambda/2\pi}{\sqrt{N_{\text{eff,TE}}^2 - n_{\text{s}}^2}} \tag{8}$$

for the TE polarization, and

$$t_{\text{eff,TM}} = t + \frac{\lambda/2\pi}{q_{\text{c}}\sqrt{N_{\text{eff,TM}}^2 - n_{\text{c}}^2}} + \frac{\lambda/2\pi}{q_{\text{s}}\sqrt{N_{\text{eff,TM}}^2 - n_{\text{s}}^2}} \tag{9}$$

for the TM polarization, with

$$q_{c,s} \equiv \left(\frac{N_{\text{eff,TM}}}{n_w}\right)^2 + \left(\frac{N_{\text{eff,TM}}}{n_{c,s}}\right)^2 - 1. \tag{10}$$

At this point, the reflectance, R, is the sole variable that remains to be determined for the absorbance calculation in (6). The specific calculations of R, and thus A, for the case of bulk solution absorption or surface-immobilized chromophores are described below.

2.1.1 Absorbance from Bulk Solution Species

Figure 3 illustrates a planar waveguide with an absorbing cover medium; light absorption in the cover medium is described by introducing an imaginary term k_c (known as extinction coefficient) to the refractive index. By using the Fresnel reflection coefficient at the waveguide-cover interface and considering the previous assumption of a weakly absorbing medium, $(k_c/n_c) \ll 1$, the reflectance, R, for each polarization is calculated. After those results are inserted into (6), the expression for the absorbance, A_b, as measured through a guided mode probing an absorbing bulk solution, is given by [8]

$$A_b = \varepsilon_b\, c_b\, \frac{\lambda}{4\pi \left(N_{\text{eff,TE}}^2 - n_c^2\right)^{1/2}} \left\{ \frac{2\, n_c \left(n_w^2 - N_{\text{eff,TE}}^2\right)}{t_{\text{eff,TE}}\, N_{\text{eff,TE}} \left(n_w^2 - n_c^2\right)}\, L \right\} \tag{11}$$

for TE modes and

$$A_b = \varepsilon_b\, c_b\, \frac{\lambda}{4\,\pi \sqrt{N_{\text{eff,TM}}^2 - n_c^2}} \left\{ \frac{2\, n_c\, n_w^2 \left(n_w^2 - N_{\text{eff,TM}}^2\right) \left(2\, N_{\text{eff,TM}}^2 - n_c^2\right)}{t_{\text{eff,TM}}\, N_{\text{eff,TM}} \left[n_w^4 \left(N_{\text{eff,TM}}^2 - n_c^2\right) + n_c^4 \left(n_w^2 - N_{\text{eff,TM}}^2\right) \right]}\, L \right\} \tag{12}$$

for TM modes. In (11) and (12), we have made use of the following relation:

$$\varepsilon_b\, c_b = \frac{4\,\pi\, k_c}{\lambda\, \ln(10)} \tag{13}$$

where ε_b is the molar absorptivity of the chromophore and c_b is its solution concentration. Equation (13) relates the notations typically used in chemistry and in optics.

2.1.2 Absorbance from Surface-Immobilized Anisotropic and Isotropic Chromophores

Next, we consider the absorbance due to a dichroic adlayer adsorbed onto the waveguide surface with the optical constants as indicated in Fig. 4. The optical properties of the dichroic layer are described by the different extinction coefficients k_x, k_y, and k_z in each Cartesian direction. The reflectance of the waveguide-adlayer-cover system follows the analysis found in Macleod [9] with the anisotropic coefficients taken from Horowitz and Mendes [10]. By assuming a thin and weakly absorbing adlayer, the following expressions are obtained for the absorbance as measured through a guided mode at each polarization [8]:

$$A_l = \varepsilon_l \Gamma_l \left\{ \frac{2\, n_l f_y \left(n_w^2 - N_{\text{eff,TE}}^2 \right)}{t_{\text{eff,TE}}\, N_{\text{eff,TE}} \left(n_w^2 - n_c^2 \right)} \; L \right\} \tag{14}$$

for TE modes, and

$$A_l = \varepsilon_l \Gamma_l \left\{ \frac{2\, n_l\, n_w^2 \left(n_w^2 - N_{\text{eff,TM}}^2 \right) \left[\left(N_{\text{eff,TM}}^2 - n_c^2 \right) f_x + (n_c/n_l)^4 N_{\text{eff,TM}}^2 f_z \right]}{t_{\text{eff,TM}}\, N_{\text{eff,TM}} \left[n_w^4 \left(N_{\text{eff,TM}}^2 - n_c^2 \right) + n_c^4 \left(n_w^2 - N_{\text{eff,TM}}^2 \right) \right]} \; L \right\} \tag{15}$$

for TM modes. In (14) and (15), the adsorbed layer is characterized by the surface coverage Γ_l of the chromophores and the molar absorptivity ε_l of a randomly oriented ensemble of chromophores. We also have used the auxiliary variables f_α defined as $f_\alpha \equiv \frac{k_\alpha}{k_l}$ for $\alpha = \text{x,y,z}$, which is the ratio of the extinction coefficient along a coordinate axis, k_α, and the extinction coefficient of a randomly oriented ensemble of chromophores, k_l. This definition leads to the following relation:

$$\varepsilon_l \Gamma_l f_\alpha = \frac{4\pi h}{\lambda \ln(10)} \; k_\alpha. \tag{16}$$

In the isotropic limit, we have $k_\alpha = k_l$ and $f_\alpha = 1$ for $\alpha = x, y, z$. By inserting those values into (14) and (15), we get the expressions for absorbance for the particular case of an isotropic absorbing film.

It is worth noting that, at least in the isotropic limit, the term $\varepsilon_l \Gamma_l$ corresponds to the absorbance one would measure by a direct transmission experiment. Therefore, the term inside the bracket in (14) (for TE modes) and (15) (for TM modes) corresponds to the enhancement factor of a long interaction length as provided by the waveguide; we called the term inside the bracket a sensitivity factor (S), which is dependent among other variables on the wavelength, waveguide mode, polarization, and on the distance between the input and output couplers, L. Later in this chapter, we show results of the sensitivity factor per unit length, S/L, for a typical waveguide configuration.

It is also important to consider when both bulk solution species and adsorbed species are simultaneously present in a waveguide measurement. In this case, the total measured absorbance will have a contribution from each term:

$$A = A_{\mathrm{b}} + A_{\mathrm{l}}. \tag{17}$$

The foregoing equations, in the isotropic limit, allow us to write the ratio of the absorbance values for each contribution as:

$$\frac{A_{\mathrm{l}}}{A_{\mathrm{b}}} = \frac{\varepsilon_{\mathrm{l}}\,\Gamma_{\mathrm{l}}}{\varepsilon_{\mathrm{b}}\,c_{\mathrm{b}}\,\frac{\lambda}{4\pi\sqrt{N_{\mathrm{eff}}^2 - n_{\mathrm{c}}^2}}}. \tag{18}$$

When the adsorption process does not significantly change the molecular molar absorptivity (in other words, $\varepsilon_{\mathrm{l}} \cong \varepsilon_{\mathrm{b}}$), then:

$$\frac{A_{\mathrm{l}}}{A_{\mathrm{b}}} \cong \frac{\Gamma_{\mathrm{l}}}{c_{\mathrm{b}}}\,\frac{4\pi\sqrt{N_{\mathrm{eff}}^2 - n_{\mathrm{c}}^2}}{\lambda} = K_{\mathrm{ads}}\,\frac{4\pi\sqrt{N_{\mathrm{eff}}^2 - n_{\mathrm{c}}^2}}{\lambda}, \tag{19}$$

where K_{ads} is the equilibrium constant between the surface-adsorbed and the bulk-dissolved species. By inserting the values of K_{ads} and λ, one can determine if the contribution of bulk species to the overall absorbance measurement is negligible or not.

2.2 Generalization to Multilayer Integrated Optical Waveguides

An electro-active planar optical waveguide (even in the single-mode regime) is typically a multilayer structure composed of a layer whose primary function is to confine the light beam and an additional conductive layer to provide an electrochemically active surface. Therefore, the usual three-medium configuration (one layer surrounded by two semi-infinite media) is insufficient for the analysis of electro-active waveguides, so we describe next a methodology more suitable to the general scenario. The approach taken here follows the work of Offersgaard [11]. For completeness and aiming to simplify his formalism for the application in hand, the following equations describe the major steps of his technique. For detailed information, the reader should refer to the original article. In general terms, the goal here is to implement a rigorous formalism where all the layers involved in the waveguide structure are included from the beginning and to solve for the bound modes in an arbitrary multilayer, dichroic, and birefrigent waveguide structure. Each layer is described by the complex refractive index n_{x}, n_{y}, and n_{z} along each Cartesian component, and the layer thickness $d^j \equiv z^{(j)} - z^{(j-1)}$. For each allowed mode and polarization, the effective refractive index of the overall structure and the associated field profile across the structure are the key pieces of information to be

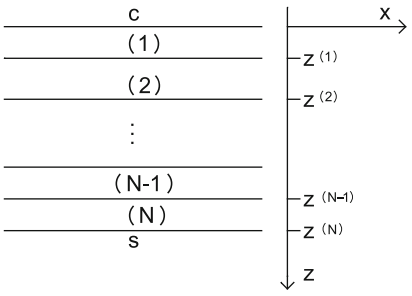

Fig. 5 Coordinate system and multilayer representation

obtained. Once in hand, the imaginary part of the effective refractive index will then determine the attenuation (absorbance) of the propagating beam of the particular waveguide mode.

In Fig. 5, we indicate the coordinate system and the notation used to model the waveguide configuration. The electric and magnetic fields are decomposed into two traveling waves: a positive ($\mathbf{E}_1$, $\mathbf{H}_1$) and a negative ($\mathbf{E}_2$, $\mathbf{H}_2$) propagating wave along the z-direction. Thus, for each medium j we write:

$$\mathbf{E}^{(j)}(\mathbf{r},t) = \mathbf{E}_1^{(j)}(\mathbf{r},t) + \mathbf{E}_2^{(j)}(\mathbf{r},t), \tag{20}$$

$$\mathbf{H}^{(j)}(\mathbf{r},t) = \mathbf{H}_1^{(j)}(\mathbf{r},t) + \mathbf{H}_2^{(j)}(\mathbf{r},t). \tag{21}$$

Each traveling component is described by:

$$\mathbf{E}_{1,2}^{(j)}(\mathbf{r},t) = \frac{1}{2}\,\psi_{1,2}^{(j)}\,\mathbf{p}_{1,2}^{(j)}\,\exp\Big\{\,i\left[\mathbf{k}_{1,2}^{(j)}.(\mathbf{r} - z^{(j)}\mathbf{e}_z) - \omega\,t\right]\Big\} + c.c., \tag{22}$$

$$\mathbf{H}_{1,2}^{(j)}(\mathbf{r},t) = \frac{1}{2}\,\psi_{1,2}^{(j)}\,\mathbf{q}_{1,2}^{(j)}\,\exp\Big\{\,i\left[\mathbf{k}_{1,2}^{(j)}.(\mathbf{r} - z^{(j)}\mathbf{e}_z) - \omega\,t\right]\Big\} + c.c., \tag{23}$$

where $c.c.$ represents the complex conjugate, ψ represents the wave amplitude, $\mathbf{p}$ and $\mathbf{q}$ are the polarization vectors, $\mathbf{k}$ is the wave vector, ω is the optical angular frequency, and $\mathbf{e}_z$ is a unit vector along the z-axis. The Faraday equation $\nabla \times \mathbf{E} = -\mu_0 \frac{\partial \mathbf{H}}{\partial t}$ relates the polarization vectors $\mathbf{p}$ and $\mathbf{q}$ through the wave vector $\mathbf{k}$:

$$\mathbf{q}_{1,2}^{(j)} = \frac{\mathbf{k}_{1,2}^{(j)} \times \mathbf{p}_{1,2}^{(j)}}{\omega\,\mu_0}, \tag{24}$$

where μ_0 is the permeability of free space. For light propagation in the x–z plane, the wave vectors may be written as:

$$\mathbf{k}_1^{(j)} \equiv \frac{2\,\pi}{\lambda}\begin{pmatrix}\beta\\0\\\alpha^{(j)}\end{pmatrix}, \tag{25}$$

$$\mathbf{k}_2^{(j)} \equiv \frac{2\pi}{\lambda}\begin{pmatrix}\beta\\0\\-\alpha^{(j)}\end{pmatrix}, \tag{26}$$

where λ is the light wavelength in vacuum. From the boundary conditions for the tangential field components, we get:

$$\begin{pmatrix}\psi_1^{(c)}\\\psi_2^{(c)}\end{pmatrix} = \mathbf{M}\,.\begin{pmatrix}\psi_1^{(s)}\\\psi_2^{(s)}\end{pmatrix}, \tag{27}$$

with:

$$\mathbf{M} \equiv (\mathbf{D}^{(c)})^{-1}\left(\prod_{j=1}^{N}\mathbf{G}^{(j)}\right)(\mathbf{D}^{(s)}), \tag{28}$$

$$\mathbf{G}^{(j)} \equiv \begin{pmatrix}\cos\left(\frac{2\pi}{\lambda}\alpha^{(j)}d^{(j)}\right) & -i\frac{p_{t1}^{(j)}}{q_{t1}^{(j)}}\sin\left(\frac{2\pi}{\lambda}\alpha^{(j)}d^{(j)}\right)\\ -i\frac{q_{t1}^{(j)}}{p_{t1}^{(j)}}\sin\left(\frac{2\pi}{\lambda}\alpha^{(j)}d^{(j)}\right) & \cos\left(\frac{2\pi}{\lambda}\alpha^{(j)}d^{(j)}\right)\end{pmatrix}, \tag{29}$$

$$\mathbf{D}^{(j)} \equiv \begin{pmatrix}p_{t1}^{(j)} & p_{t2}^{(j)}\\ q_{t1}^{(j)} & q_{t2}^{(j)}\end{pmatrix}. \tag{30}$$

In (29) and (30), the subscript t refers to the tangential components of the corresponding vector.

For the TE polarization, the tangential component of the polarization vectors is given by:

$$p_{y1} = p_{y2} = 1, \tag{31}$$

and application of (24) gives us:

$$q_{x1} = -q_{x2} = -\sqrt{\frac{\varepsilon_0}{\mu_0}}\,\alpha, \tag{32}$$

where ε_0 is the permittivity of free space.

As previously described, we assume a diagonal tensor for the permittivity

$$\frac{\varepsilon}{\varepsilon_o} = \begin{pmatrix}n_x^2 & 0 & 0\\ 0 & n_y^2 & 0\\ 0 & 0 & n_z^2\end{pmatrix}, \tag{33}$$

which can describe most of the experimental configurations of interest. By inserting (33) into the wave equation, we get

$$\left[\frac{\varepsilon}{\varepsilon_0} - \left(\frac{c}{\omega}\right)^2 |\mathbf{k}|^2\right]\mathbf{E} + \left(\frac{c}{\omega}\right)^2 (\mathbf{k}\cdot\mathbf{E})\,\mathbf{k} = 0, \tag{34}$$

so we can relate both components of the wave vector by the dispersion equation:

$$\alpha = \sqrt{n_{\mathrm{y}}^2 - \beta^2}, \tag{35}$$

where the root, to provide decaying fields far from the guide, should be chosen according to:

$$\mathrm{Im}\,(\alpha) > 0. \tag{36}$$

For the TM polarization, we find the tangential components of the polarization vector are given by:

$$p_{x1} = -p_{x2} = \frac{\alpha}{\sqrt{\left|\beta\,(n_x/n_z)^2\right|^2 + |\alpha|^2}}, \tag{37}$$

and

$$q_{\mathrm{y1}} = q_{\mathrm{y2}} = -\sqrt{\frac{\varepsilon_0}{\mu_0}}\frac{(n_{\mathrm{x}})^2}{\sqrt{\left|\beta\,(n_{\mathrm{x}}/n_{\mathrm{z}})^2\right|^2 + |\alpha|^2}}. \tag{38}$$

Again, the wave equation relates the components of the wave vector by:

$$\alpha = \frac{n_{\mathrm{x}}}{n_{\mathrm{z}}}\sqrt{n_{\mathrm{z}}^2 - \beta^2}, \tag{39}$$

where the root should also be chosen according to (36).

The determination of β, the only remaining unknown, is provided by solving

$$m_{11}(\omega, \beta) = 0 \tag{40}$$

to produce a bound mode in the waveguide region; m_{11} is an element of the matrix defined in (28). After denoting the solution to (40) as

$$\beta_0 = N_{\mathrm{Re}} - i\,N_{\mathrm{Im}}, \tag{41}$$

the absorbance is calculated as:

$$A = \frac{4\,\pi\,L}{\lambda\,\ln 10} N_{\mathrm{Im}}. \tag{42}$$

2.3 Sensitivity of Single- and Multimode Waveguide Structures

Operation of planar waveguides in the single-mode regime offers several advantages when compared with multimode configurations in applications of absorbance spectroscopy. Most importantly, the sensitivity for probing chromophores in proximity of the waveguide surface is far superior in the single-mode structure compared with the multimode structure. As a metric to quantify this point, Fig. 6 shows the sensitivity factor per unit length, S/L, defined as the absorbance per unit length, A_l/L, measured through a guided mode propagating for a distance L inside the waveguide divided by the absorbance measurement in direct transmission configuration, $\varepsilon_l \Gamma_l$, for probing a surface-adsorbed thin film. For convenience, the data are plotted with the V-number as the x-axis, which is related to the waveguide thickness by: $V = \frac{2\pi t \sqrt{n_w^2 - n_s^2}}{\lambda}$. For small thicknesses (small V-number), the waveguide operates in the single-mode regime and the sensitivity reaches a peak at approximately $V = 1.53$ for TE and $V = 1.73$ for TM. Below the peak, as V-number decreases and N_{eff} approaches n_s, the Goos-Hanchen shift effect dominates the effective thickness and makes the guided modes excessively large, decreasing the sensitivity. As the thickness increases beyond the ideal V-number, the sensitivity of the lowest-order mode decreases rapidly. At the same time, new modes are allowed to propagate in

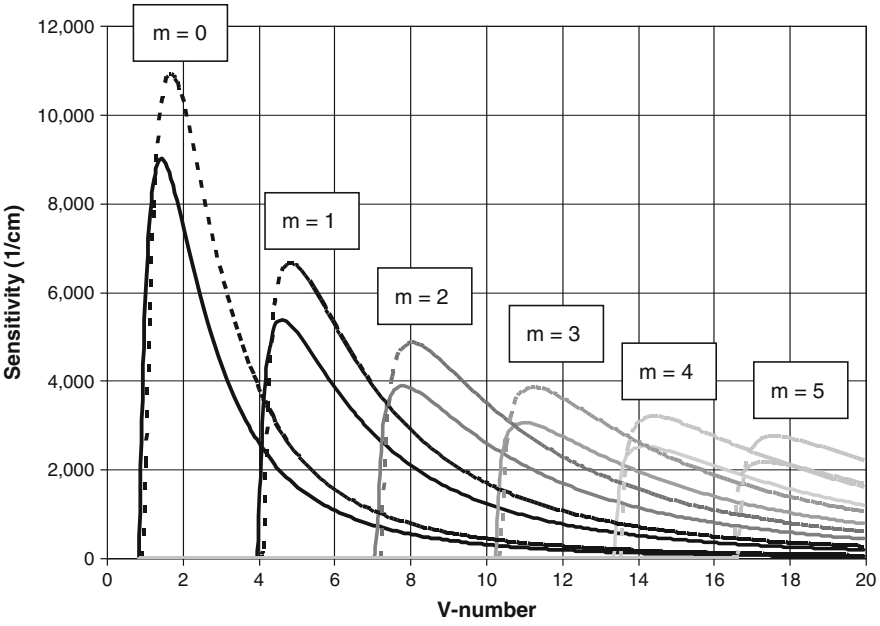

Fig. 6 Sensitivity factor per unit length for absorbance measurement through propagating guided modes. Refractive index profile is given by 1.33 (water cover), 1.56 (waveguide film; e.g. Corning glass 7059), and 1.46 (fused silica substrate). *Solid lines*: TE modes; *dashed lines*: TM modes. Wavelength for calculations: $\lambda = 550$ nm

the guiding structure; however, their sensitivity is much less than that in the single-mode regime.

Another complicating factor in multimode waveguides is that the sensitivity needs to be evaluated by the weighted average of all the modes that propagate in the structure; the weighting factor measures the fraction of optical power coupled into each mode. Therefore, in order to retrieve any information from measurements with a multimode waveguide, a precise knowledge of the power distribution at the input coupling port is required. An additional complication for multimode waveguides is that power hopping from mode to mode is always present to some degree because of scattering mechanisms along the propagation length of the guide, and this can also disturb the retrieved information.

2.4 Polarized Measurements and Molecular Orientation

Electromagnetic radiation of any frequency is described by the interplay of oscillating electric and magnetic fields, which are vectors and therefore require a direction in space for a full description. The optical absorption of an electromagnetic wave by matter is determined by specifying the electric field vector associated with the electromagnetic radiation and the vector transition dipole for the molecule under investigation. As expressed in the Fermi's Golden rule,

$$A = \left\langle \left| \vec{\mu}.\vec{E} \right|^2 \right\rangle. \tag{43}$$

By controlling the orientation in space of the probing electric field, one can gain information on the orientation of the transition dipoles being probed by the light beam. Usually, that information is described as an order parameter, which is intrinsically an ensemble average over the population of molecules interacting with the light beam. If one then knows the relationship between the transition dipole with respect to the molecular structure (e.g., the transition dipole angle with respect to the molecular plane of a polyaromatic hydrocarbon) it is possible to infer the molecular orientation in space.

Optical modes of different polarizations (TE or TM) in planar waveguides interact differently with chromophores located in the proximity to the waveguide surface. Typically, the electric fields associated with TE and TM modes have different strengths at the interface and different profiles across the waveguide structure, and those features lead to different optical interaction with the absorbing species even when those species are isotropically (or randomly) distributed in space. Equations (14) and (15) provide a quantitative description of those effects and it is common to say that the pathlength for TE and TM are different. For a simple and well-defined waveguide structure (e.g., the step-index single-layer waveguide), it is possible to derive analytical expressions as described in Sect. 2.2. In the case more of complex structures (e.g., multilayer and/or gradient-index), a complete and

accurate description of the waveguide for predicting the behavior of TE and TM can be difficult. A simplifying approach that is particularly useful in these difficult cases, and is also applicable in general, is to initially calibrate the planar waveguide with an isotropic probe, which can be either an absorbing species dissolved in the bulk phase or a thin-film that is known to have random dipole orientation when immobilized on the waveguide. By measuring the absorbance at both polarizations for such an isotropic probe, we can factor out the difference in pathlength that is due to solely to the difference in the electric fields of the TE and TM modes. With such calibration in hand, one can then apply the calibrated waveguide to samples of interest. As previously described [12], the normalized dichroic ratio defined by

$$\rho_{\text{norm}} \equiv \frac{\rho_{\text{sample}}}{\rho_{\text{iso}}} = \frac{\left(A_{\text{TE}}/A_{\text{TM}}\right)_{\text{sample}}}{\left(A_{\text{TE}}/A_{\text{TM}}\right)_{\text{iso}}} \tag{44}$$

can be related to the dipole components along the Cartesian axes using

$$\rho_{\text{norm}} = \frac{\left\langle \mu_{\text{y}}^2 \right\rangle \left(2N_{\text{eff,TM}}^2 - n_{\text{c}}^2\right)}{\left\langle \mu_{\text{x}}^2 \right\rangle \left(N_{\text{eff,TM}}^2 - n_{\text{c}}^2\right) + \left\langle \mu_{\text{z}}^2 \right\rangle N_{\text{eff,TM}}^2}, \tag{45}$$

with a numerical value bound as follows:

$$0 \leq \rho_{\text{norm}} \leq \frac{2N_{\text{eff,TM}}^2 - n_{\text{c}}^2}{N_{\text{eff,TM}}^2 - n_{\text{c}}^2}. \tag{46}$$

From the normalized dichroic ratio, one can calculate the dipole component along each Cartesian axis (in = x, y; out = z) as:

$$\frac{\left\langle \mu_{\text{in}}^2 \right\rangle}{\mu^2} = \frac{1}{2} - \frac{\left\langle \mu_{\text{out}}^2 \right\rangle}{2\,\mu^2} = \frac{\rho_{\text{norm}} N_{\text{eff,TM}}^2}{\left(2N_{\text{eff,TM}}^2 - n_{\text{c}}^2\right) + \rho_{\text{norm}}\left(N_{\text{eff,TM}}^2 + n_{\text{c}}^2\right)}, \tag{47}$$

from which the order parameter associated with the one photon process (absorption) can be calculated by [13]:

$$\langle P_2(\theta) \rangle = \frac{3\left\langle \mu_{\text{out}}^2 \right\rangle}{2\,\mu^2} - \frac{1}{2} \tag{48}$$

For a more comprehensive description of the molecular orientation, higher-order parameters are typically needed to add independent information for the reconstruction of a probability distribution function [14]. The ability to detect molecular orientation changes during ET events of surface-confined molecules is an extremely

powerful capability afforded by the use of electro-active waveguides. It has often been suspected that addition or subtraction of an electron from an isolated molecule on a surface would be accompanied by, and controlled by, an orientation change of that molecule.

3 Instrumental Setup

Optical spectroscopy with single-mode planar waveguide requires bright light sources (high power per mode), sensitive detectors, and efficient waveguide couplers. Furthermore, these optical components need to perform well over a broad spectral band. Current detector technologies, either single-channel detectors (e.g., avalanche photodiode, photomultiplier) or array detectors (CCD) are generally suitable. Input and output optical waveguide couplers capable of handling broadband light sources that are spatially incoherent (composed of a large number of spatial modes) with limited brightness are certainly a major challenge for the implementation of broadband spectroscopy with single-mode planar optical waveguides for interrogation of molecular films.

3.1 Waveguide Couplers

Input and output couplers for single-mode planar optical waveguides can be broadly classified as end-facet couplers or transverse couplers. End-facet couplers work quite well in particular for channel waveguides with cross-sectional dimensions of a few microns in height and width [15]. However, for waveguides with submicron dimensions in the transverse direction, the end-facet approach is problematic as it requires the formation of a smooth and optically flat facet right at the very end of the waveguide device. In those cases, transverse couplers such as prism and grating couplers are usually the preferred choice.

3.1.1 Prism Coupler

A prism in close proximity to a waveguide film can be used to excite waveguide modes [16] as long as the prism's refractive index is higher than the effective index of the particular guided mode. As shown in Fig. 7, the effective refractive index of the coupler (also know as Snell invariant, $N_p = n_p \sin\theta_p$, and defined as the projection of the k-vector of the incoming beam onto the waveguide surface divided by $2\pi/\lambda$) is given by:

$$N_p = n_p \sin\theta_p = n_i \sin\theta_i \cos\varphi + \sqrt{{n_p}^2 - {n_i}^2 \sin^2\theta_i}\ \sin\varphi, \tag{49}$$

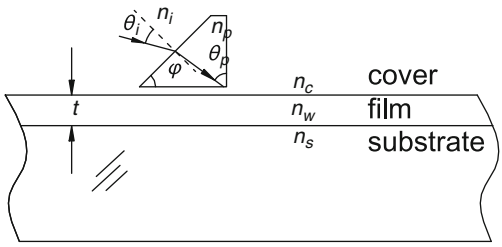

Fig. 7 Input prism coupler

where φ is the prism base angle. By tuning the angle θ_i of the incident beam, one can adjust the coupler effective index N_p to match the effective refractive index of the waveguide, i.e.,

$$N_\mathrm{p} = N_\mathrm{eff}. \tag{50}$$

As previously discussed, N_{eff} is found for each mode and polarization by solving either (1) in the case of a single-layer waveguide or (40) for the more complex configurations.

The effective refractive indices of the waveguide $N_\mathrm{eff}(\lambda)$ and the prism coupler $N_\mathrm{p}(\lambda)$ depend on the wavelength. In the case of the prism coupler, the dispersion of $N_\mathrm{p}(\lambda)$ comes from the material dispersion as expressed in (49); in the case of the waveguide effective refractive index, the material dispersion is also important but an additional major contribution to the overall dispersion comes from the mode confinement (known as modal dispersion) which can be seen by the explicit wavelength dependence of (1). Typically, for a particular angle of incidence of the incoming broadband beam, only a center wavelength and a small band around it will give an efficient match between the coupler and the waveguide effective refractive index. In general, either the angle needs to be tuned to couple different wavelengths or an angular width (also known as numerical aperture, NA) in the optical beam needs to be provided to achieve broadband operation. An incident beam with an appropriate angular width was the approach taken by Kato et al. [17] and Bradshaw et al. [3, 18] to achieve broadband coupling in single-mode planar optical waveguides. Prisms with a proper dispersive power can also be designed to match the dispersion behavior between coupler and waveguide, and therefore significantly reduce the angular width needed to couple a broader spectral range [19].

3.1.2 Grating Coupler

The effective refractive index, N_g, of a diffraction grating coupler, as illustrated in Fig. 8, is described by [20–22]:

$$N_\mathrm{g} = n_\mathrm{i} \sin\theta_\mathrm{i} + m\,\frac{\lambda}{\Lambda}\,, \tag{51}$$

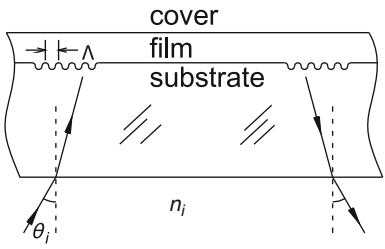

Fig. 8 Input and output grating couplers

where the first term in the right-hand side accounts for the Snell invariant, Λ is the grating period, and m is the period of the grating. As before, the effective refractive index of the coupler needs to match that of the waveguide mode, i.e.,

$$N_{\mathrm{g}} = N_{\mathrm{eff}}, \tag{52}$$

which is done by tuning the angle θ_{i} for each wavelength. Unlike the prism coupler, the grating coupler can be implemented with the beam illumination either from the top side or from the bottom side of the device.

Grating couplers are typically integrated into the waveguide device and buried underneath the waveguide layer by first creating a periodic corrugation on the surface of the substrate slide and then depositing the waveguide layer. This process of creating a surface corrugation in the substrate usually involves the fabrication of a holographic pattern, done in a Lloyd's mirror configuration, to imprint an interference pattern in a photoresist film deposited on the substrate. The photoresist film is developed to create a photopattern with a periodic modulation. Dry etching of the photopattern is then employed to transfer the modulation to the substrate slide. After removal of any remaining photoresist, the samples with the periodic corrugation are then overcoated with the waveguide structure of choice [23].

Unlike the prism coupler which requires precise alignment of an extra external optical element to excite a guided mode, grating couplers are fully embedded in the optical device and simplify tremendously its incorporation into a spectroscopic instrument. As mentioned above, both grating and prism couplers require the adjustment of the incoming optical beam to the proper angle to match the effective index of the coupler and the waveguide; in addition, both couplers require the lateral position of the optical beam to be located close to the edge of the coupler to achieve strong coupling efficiencies [24].

Comparing the prism coupler to the grating coupler, the former has the advantage of low dispersion and therefore requires a smaller NA for achieving broadband coupling. An inconvenience, however, is the requirement of mounting the prism in close proximity to the waveguiding layer, separated by a very small (in the wavelength range) and precisely fixed gap. Changes in the gap affect the coupling efficiency substantially and perturb the measurements. Although grating couplers are fully integrated optical components that provide strong robustness to the coupling process, they require either a scanning angle capability or a very high NA to achieve broadband operation.

3.1.3 Achromatic Coupler

An approach that aims to overcome the difficulties above involves the combination of a grating coupler with two pre-dispersive components: an additional grating and a prism to minimize the overall mismatch between the coupler and waveguide effective indices [25]. The additional grating is designed to approximately cancel the dispersion of the grating coupler; the prism is added solely to improve the cancellation of the effective index mismatch and is optically attached to the back side of the device without requiring stringent control of the gap. In this case, broadband operation with single-mode waveguides was achieved and demonstrated for submonolayer protein films [26].

3.2 Broadband Light Sources and Lasers

Let us now consider spectroscopic measurements over a broad spectral band, such as that emitted by a blackbody source. A typical tungsten–halogen lamp operated at a temperature of 3,200 K in the tungsten filament (with an emissivity of 0.33) has an emission spectrum with a power density of about −75 dBm/nm per mode (or 33 pW/nm per mode) around the center of the visible spectrum (550 nm). Such low brightness, expressed either by the optical power/(unit wavelength × mode) or by optical power/(unit wavelength × emitting area × solid angle), identifies a major challenge for using typical broadband light sources with planar waveguides operating in the single-mode regime at the transverse direction of the guiding structure.

The maximum power that can be coupled into each mode of a waveguide structure is given by the power per mode emitted by the light source being deployed. Passive optical components (without a gain medium as in lasers or optical amplifiers) cannot increase the brightness of an optical beam; the best they can do is sustain the power per mode of an incoming beam. In channel waveguides and optical fibers, with both transverse and lateral confinements, one can calculate the total number of modes for the particular structure and estimate the maximum power that can be coupled into the device. In slab planar waveguides, with confinement only in the transverse direction, one can increase the device throughput by launching several modes in the lateral dimension. Although in this case, the sensitivity for probing surface events is approximately the same for all the lateral modes, an enhanced throughput can be quite helpful in increasing the signal-to-noise ratio of the spectroscopic measurement. In other words, a single-mode slab optical waveguide corresponds to several hundreds (or even thousands) of channel waveguides, all of them probing simultaneously surface-adsorbed species with equal sensitivity.

Regarding the source brightness, tunable lasers are certainly an alternative for overcoming the low brightness of incoherent sources; however, their higher cost can be a limiting factor for several applications. The arrival of GaN LED

technologies at shorter wavelengths in the visible spectrum and into the near UV may become a useful alternative for the applications discussed here, as they may provide higher brightness than broadband filament or arc lamp sources. Although LED brightness is lower than that of lasers, they offer broader spectral emission which partially circumvents the need for tunability in laser sources. We also note the emergence of new technologies such as supercontinuum generation and amplified spontaneous emission (ASE) that can potentially offer new alternatives for higher brightness broadband sources to be incorporated into waveguide spectroscopic instrumentation.

When photometric detection with a single wavelength or narrow band is sufficient, spatially coherent (spatially single-mode) laser sources are the preferred choice as they offer high brightness and are easily coupled into single-mode optical waveguides. Because of the high brightness of readily available laser beams and the simplicity in setting up a waveguide coupler for a single wavelength, the majority of applications with single-mode integrated optical waveguides have been limited to single wavelength measurements. However, in many of those cases, acquisition of broadband spectroscopic data would be much preferred to enable molecular structure to be characterized and overlapping spectral signals of multiple chromophores to be resolved.

3.3 *Electro-Active Optical Waveguides: Materials and Fabrication*

Itoh and Fujishima were among the first to perform both photometric and electrochemical interrogations on an electro-active planar optical-waveguide platform [27, 28]. In their 1988 report, they described a channel gradient-refractive-index glass waveguide fabricated by the ion exchange process and overcoated by spray pyrolysis with an electro-active, antimony-doped, tin oxide layer to provide for both electrochemical and optical detection of surface-adsorbed species. Simultaneous acquisition of the cyclic voltammogram and the corresponding intensity of an outcoupled beam from a propagating guided wave excited with a 633 nm He-Ne laser were obtained for an adsorbed layer of methylene blue (MB). MB is a convenient redox couple with which the sensitivities of thin waveguide platforms with the original ATR-based spectroelectrochemical platforms can be compared. MB adsorbs to oxide surfaces and has a well-known, reversible two-electron reduction at -0.275 V and a high-molar absorptivity for the oxidized form at 633 nm, so that probing its activity with conventional He–Ne lasers is straightforward.

Itoh and Fujishima reported a sensitivity factor for the optical signal of 20–40 for a multimode structure and approximately 150 for a single-mode waveguide [27, 28]. These sensitivity factors are consistent with the weak confinement provided by a gradient-refractive index waveguide. Another relevant work was

reported by Piraud et al. on the development of a chemical sensor based on the opto-electrochemical response of an electro-active ion-exchange channel waveguide overcoated with a redox active film [29, 30].

As described above, ion-exchange waveguides certainly provide enhanced sensitivity when compared with optical interrogation in direct transmission geometry. However, their signal enhancement is characteristically less than what can be achieved by a step-refractive index profile. As shown in Fig. 6, a typical step-refractive index single-mode waveguide with submicron optical confinement provides several orders of magnitude (about 9,000/cm for TE and 11,000/cm for TM in the example of Fig. 6) in sensitivity enhancement per centimeter of beam propagation along the device.

To achieve higher sensitivity, Dunphy et al. [4, 5] developed a planar single-mode electro-active waveguide. Although formed by a stack of three layers (each layer with a constant refractive index), the optical device was designed and fabricated to operate in the single-mode regime with tight optical confinement, and thus high sensitivity. As schematically shown in Fig. 9, the multilayer electro-active waveguide structure consisted of Corning 7059 glass, silicon dioxide, and indium tin oxide (ITO) layers that were deposited on a soda lime glass substrate (75mm $\times$ 25mm $\times$ 1 mm) using a RF sputtering technique. The primary function of the Corning glass layer (refractive index $n = 1.56$, thickness $t = 400$ nm) is to provide for most of the optical confinement. The next layer, SiO_2, with $n = 1.46$ and $t = 200$ nm, functions as a buffer to minimize possible ion migration between the Corning glass layer and the overlying ITO layer; such migration could result in greater optical propagation losses and reduced electrical conductivity in the ITO layer. The ITO layer, with $n = 2.0$ and $t = 50$ nm, was deposited under optimized partial pressure of O_2 to achieve an appropriate balance of optical transparency and electrical conductivity. After RF sputtering deposition, an annealing process was performed at 225°C to improve the ITO conductivity by reducing grain boundary defects. For a 50-nm-thick ITO layer, Dunphy et al. [4, 5] reported resistance values of 700−800 Ω/□.

As illustrated in Fig. 9 and described in Sect. 3.1.2, prior to sputtering deposition of the layers, two surface relief gratings (period of $\Lambda = 400$ nm) were fabricated on the glass slide for input and output coupling of the optical beam. A calculation based on the theory developed in Sect. 2.2 gave an electric field profile for the TE mode as shown in Fig. 10.

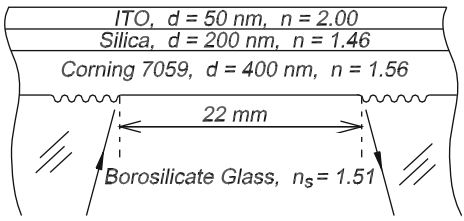

Fig. 9 Electro-active planar single-mode optical waveguide. Adapted from [4] with permission from the America Chemical Society, copyright 1997

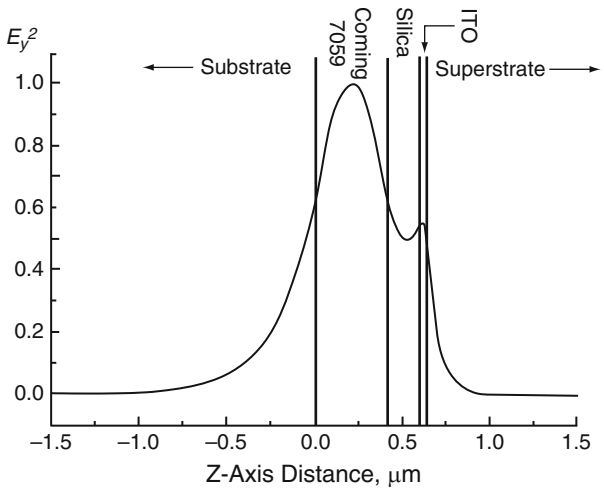

Fig. 10 Electric field profile in TE polarization across the multilayer electro-active waveguide structure. Adapted from [4] with permission from the America Chemical Society, copyright 1997

4 Characterization and Applications

4.1 Adsorbed Dyes

Dunphy et al. [4, 5] and Mendes et al.[4] first applied the electro-active single-mode waveguide (Figs. 9 and 10) for electrochemical characterization of adsorbed MB since exploration of this redox couple provided a direct comparison to the sensitivity of previously developed spectroelectrochemical platforms. Figure 11 summarizes the results. The reduction of MB to its leuco (transparent at 633 nm) form results in transmittance increase in the waveguide; however, this behavior is superimposed on a loss of transmittance arising from background changes in the optical properties of the ITO thin film with increasing negative applied potentials as shown in Fig. 11a. Hansen et al. [1] were the first to describe this phenomenon for spectroelectrochemical platforms, showing it to arise from the changes in electron density of states in the near surface region of the oxide, causing an increased light attenuation in the background signal that is almost linear with applied potential. Fortunately, this background attenuation can be easily subtracted, leaving the absorbance change versus potential shown in Fig. 11b.

The derivative of the absorbance with respect to the applied potential, $\mathrm{d}A/\mathrm{d}E$, allows one to create an absorpto-voltammogram, shown in Fig. 12 (a), where the data for $\mathrm{d}A/\mathrm{d}E$ are plotted versus the electric potential for both the forward (reduction of MB to its leuco form) and reverse (reoxidation of leuco MB to MB) sweeps. These experimental results can be quite useful when we consider that double layer charging usually does not produce major changes in the spectroscopic

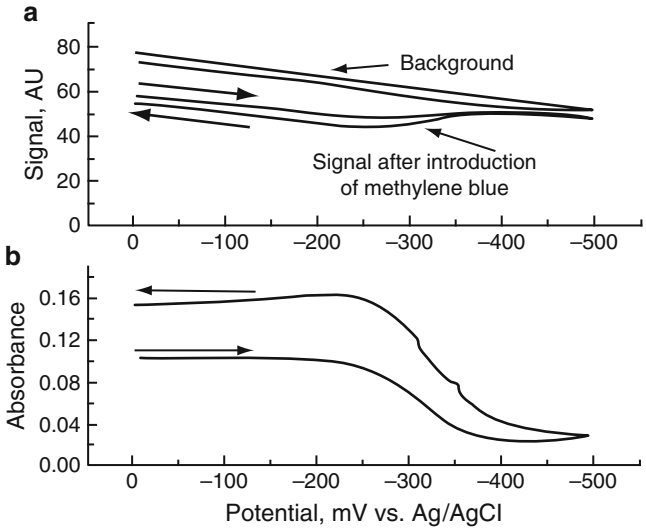

Fig. 11 (**a**) Change in the optical signal as a function of applied potential during reduction (negative going sweep) and oxidation for both solution background and a surface-confined MB submonolayer. There is a significant change in background transmittance of the ITO/waveguide platform as a function of applied potential arising from the change in free electron population in the near surface region as the electrode potential move towards negative potentials; however, these optical changes are easily removed to provide the plot shown in (**b**) for the net absorbance due solely to the redox couple. The two-electron, one-proton reduction process converts the blue form of MB to its leuco form, which is fairly transparent at the working wavelength of 633 nm. Reprinted from [5] with permission from Marcel Dekker, copyright 1999

data (or produces changes that can be easily removed), and under those conditions, the Faradaic current can be related to the optical changes in the adsorbed redox species by [31]:

$$\frac{\mathrm{d}A}{\mathrm{d}E} = \frac{S\left(\varepsilon_{\mathrm{O}} - \varepsilon_{\mathrm{R}}\right)}{n\,F\,B\,v}\; i_{\mathrm{F}}, \tag{53}$$

where n is the electric charge per molecule, F is the Faraday constant, B is the electrode area, v is the scan rate, E is the applied potential, S is the waveguide sensitivity factor, and ε_{O} (ε_{R}) is the molar absorptivity of the oxidized (reduced) species. As described in (53), the derivative of the optical absorbance with respect to the applied potential is directly proportional to the Faradaic current, with no contribution from the non-Faradaic component. A key advantage of the optical interrogation, when compared to the conventional cyclic voltammetry, is the removal of the non-Faradaic components in the optical signal.

An electro-active integrated optical waveguide (EA-IOW) with a separation of 8 mm between the input and output grating couplers was used to experimentally assess the sensitivity of EA-IOW-based measurements on surface-confined films. Measurements performed on adsorbed MB ($\varepsilon = 7{,}800\ \mathrm{M}^{-1}\ \mathrm{cm}^{-1}$ at 633 nm) at a

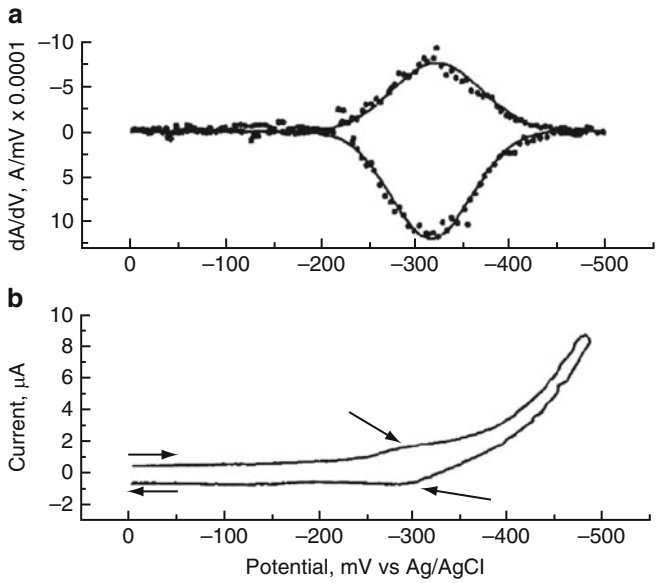

Fig. 12 (**a**) The reconstructed absorpto-voltammogram and (**b**) the original cyclic voltammogram (current versus applied voltage, as voltage is swept continuously to about −0.5 volts and back to 0.0 volts) for surface-confined MB on the ITO-coated single-mode waveguide. The cyclic voltammogram shows a nearly indistinguishable peak on the forward and reverse sweeps corresponding to the reduction and oxidation of surface-confined MB, masked by the background current associated with charging of the electrical double layer at the electrode/solution interface. The absorptovoltammogram is obtained by taking the first derivative of the background-corrected absorbance (Fig. 11) versus applied potential, and shows high contrast during the reduction of MB to the leuco (transparent) form of the dye. There is a larger optical change on the reverse sweep (oxidation of leuco form back to MB) than on the forward sweep (reduction of MB to the leuco form), which we have hypothesized arises from changes in packing density of the leuco form of the dye, once formed, leading to higher overall surface coverages. The data shown were obtained at slow sweep rates; at higher sweep rates, which did not provide time for this rearrangement, the asymmetry in the peak shapes was removed. Reprinted from [5] with permission from Marcel Dekker, copyright 1999

surface coverage of approximately 4% of a close-packed monolayer showed that the EA-IOW is about 4,000 times more sensitive than a single-pass transmission geometry, which represented a significant improvement over earlier electro-active waveguide platforms.

4.2 Spectroelectrochemistry of Cytochrome c Films

Due to potential applications in biosensing and to develop a better understanding of heterogeneous biological electron transfer reactions, direct electrochemistry between adsorbed proteins and solid electrodes has been studied extensively [32,

33]. Much of the research in this field has dealt with horse cytochrome *c* (cyt *c*), a small electron transfer protein that contains a redox-active, iron porphyrin prosthetic group [34]. It is widely hypothesized that in order for facile electron transfer to occur between surface-adsorbed cyt *c* and a solid electrode, the protein molecules must be oriented with the heme pocket facing the electrode surface [34, 35]. This favorable structure is thought to result from electrostatic interactions between the asymmetric distribution of positive charges on cyt *c* and the negatively charged electrode surface. Conventional electrochemical techniques are useful for characterizing reaction rates in these systems but cannot provide a rigorous assessment of the oriented adsorption hypothesis because they do not provide structural information.

A comparison of conventional cyclic voltammetry (CV) and EA-IOW-based spectroelectrochemistry of cyt *c* adsorbed to a waveguide surface is shown below. The CV data plotted in Fig. 13 were recorded at several scan rates [36]; even at the highest scan rate, non-Faradaic background overwhelms the Faradaic portion of the signal. An example of an absorpto-voltammogram measured on an equivalent cyt *c* film in TM polarization at 514.5 nm is shown in Fig. 14a. The corresponding reconstructed voltammogram, shown in Fig. 14b (*solid line*), demonstrates the power of EA-IOW-based spectroelectrochemistry to completely eliminate the non-Faradaic background. The optical data can also be measured using TE-polarized light, and the respective reconstructed voltammogram is plotted in Fig. 14b as well (*dotted line*). As discussed above, the ratio of the absorbances in TE and TM provides information about the orientation of the chromophores in the film (in this case, the iron porphyrin in cyt *c*). Thus, the data in Figs. 13 and 14 demonstrate that EA-IOW-based spectroelectrochemistry provides simultaneous information about both electron transfer rates and molecular orientation for ultra-thin adsorbed protein films.

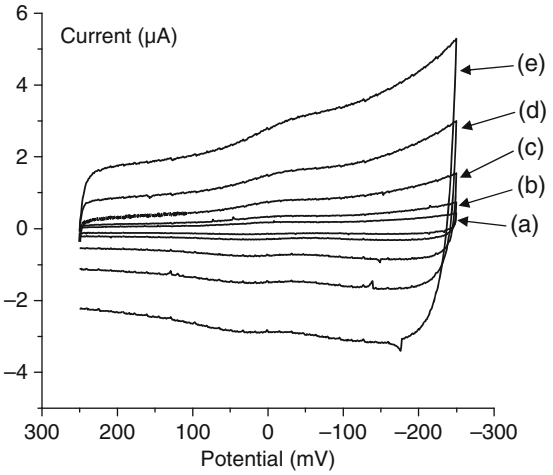

Fig. 13 Cyclic voltammograms of cyt *c* adsorbed to ITO in 5 mM, pH 7 phosphate buffer, at varying scan rates: (**a**) 10, (**b**) 20, (**c**) 50, (**d**) 100, and (**e**) 200 mV/s. The potential is reported versus an Ag/AgCl reference electrode. The protein surface coverage is about 8 pmol/cm^2; [36]

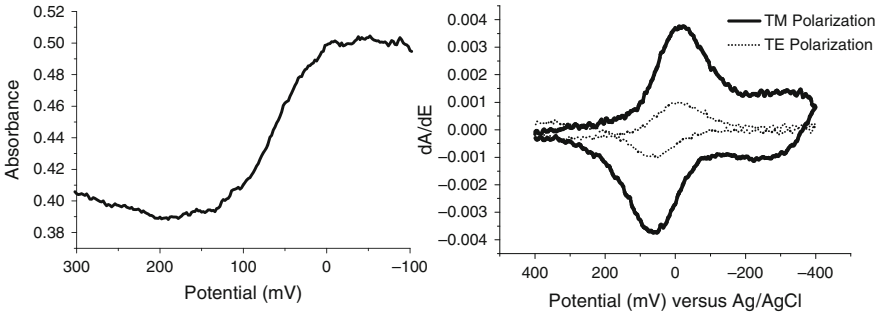

Fig. 14 (**a**) The absorbance response, measured at 514.5 nm in TM polarization, of a film of cyt *c* (about 8 pmol/cm^2) adsorbed to an EA-IOW measured during a potential scan from +400 to −400 mV. (**b**) An optically detected cyclic voltammogram (*solid line*) reconstructed from the data in (**a**). The TE-polarized, optically detected cyclic voltammogram is also shown (*dotted line*) [36]

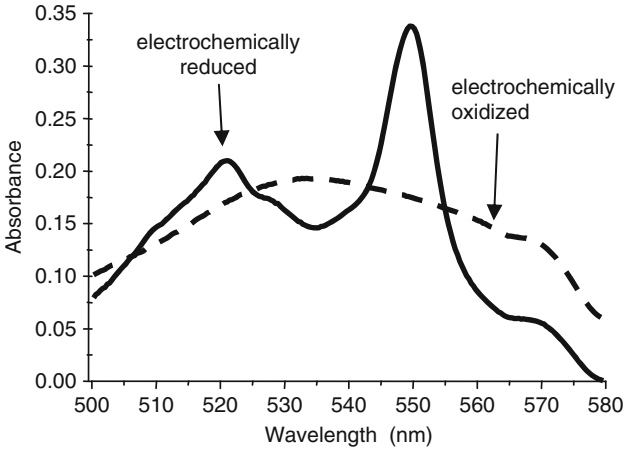

Fig. 15 TM-polarized EA-IOW spectra of a submonolayer of cyt *c* adsorbed to the surface of the EA-IOW: (1) electrochemically reduced ferrocyt *c* (*solid line*), collected at a potential of −400 mV vs. Ag/AgCl; (2) electrochemically oxidized ferricyt *c* (*dashed line*), collected after scanning the potential to +400 mV. Reprinted from [3] with permission from the America Chemical Society, copyright 2003

4.3 Broadband Spectroscopy on an EA-IOW

The studies described in Sects. 4.1 and 4.2 were performed with monochromatic laser sources. To provide the information content of broadband spectroscopy, Bradshaw et al. [3] extended the prism coupling approach of broad angular width

described above to create a broadband-coupled EA-IOW. The result is a spectrometer that combines the extreme sensitivity of the single-mode EA-IOW with a multichannel spectroscopic capability over a 200 nm spectral bandwidth.

In Fig. 15, EA-IOW spectra of an adsorbed cyt *c* layer at potentials necessary to maintain the protein in its fully reduced state or fully oxidized state are shown. Scanning to and maintaining the potential at −400 mV vs. Ag/AgCl reduces the cyt *c* layer, resulting in the appearance of the sharp band near 550 nm, which is characteristic of ferrocyt *c*. Scanning to and maintaining the potential at +400 mV oxidizes the protein, producing a spectrum with a single, broad band in the 500–600 nm range, which is characteristic of ferricyt *c*. These spectra were acquired in the TM_0 mode and the entire spectral range from ~500 to ~700 nm was probed simultaneously. Spectra can also be acquired in the TE_0 mode, which allows molecular order parameters to be measured under potential control over a broad spectral bandwidth. This combination of features is unprecedented.

5 Concluding Remarks

The sections above illustrate the combination of sensitivity and high information content that can be provided by the EA-IOW platforms. Future applications will likely include characterization of relationships between molecular structure and charge transport in ultra-thin films. The ability to study submonolayer films has the potential to yield significant insight into current problems in electrochemistry such as hypothesized relationships between molecular packing, orientation, and electron transfer kinetics. Another important application is chemical sensing based on spectroelectrochemical selectivity, e.g., sensors in which absorbance, luminescence, and an electrochemical parameter, such as current or interfacial potential, can be monitored simultaneously to produce greater orthogonality of data in response space relative to standard electrochemically based sensors (e.g., ion-selective electrodes) [37].

Current technical difficulties mostly center on fabrication challenges appropriate to combine high transparency to achieve low propagation loss and high conductivity on the surface chemistry of ITO, which is rough, chemically heterogeneous, and metastable. Instrumental difficulties in light coupling, especially for broadband interrogation with low brightness sources, would benefit from a more user-friendly apparatus to facilitate a wider range of applications.

References

1. Hansen WN, Kuwana T et al (1966) Observation of electrode-solution interface by means of internal reflection spectrometry. Anal Chem 38(13):1810–1821
2. Kuwana T, Heineman WR (1976) Study of electrogenerated reactants using optically transparent electrodes. Acc Chem Res 9(7):241–248

3. Bradshaw JT, Mendes SB et al (2003) Broadband coupling into a single-mode, electroactive integrated optical waveguide for spectroelectrochemical analysis of surface-confined redox couples. Anal Chem 75(5):1080–1088
4. Dunphy DR, Mendes SB et al (1997) The electroactive integrated optical waveguide: ultrasensitive spectroelectrochemistry of submonolayer adsorbates. Anal Chem 69(15):3086–3094
5. Dunphy DR, Mendes SB, et al (1999) Spectroelectrochemistry of monolayer and submonolayer films using an electroactive integrated optical waveguide, Chapter 29. In: Wieckowski A (Ed) Interfacial electrochemistry. Marcel Dekker, New York
6. Tien PK (1971) Light waves in thin films and integrated optics. Appl Opt 10(11):2395–2413
7. Kogelnik H (1979) Theory of dielectric waveguides. Integrated optics, 2nd edn. New York, Springer, pp 13–81
8. Mendes SB, Saavedra SS (2000) Comparative analysis of absorbance calculations for integrated optical waveguide configurations by use of the ray optics model and the electromagnetic wave theory. Appl Opt 39(4):612–621
9. Macleod HA (1986) Thin-film optical filters. Macmillan, New York
10. Horowitz F, Mendes SB (1994) Envelope and wave-guide methods – a comparative-study of PbF2 and CeO2 birefringent films. Appl Opt 33(13):2659–2663
11. Offersgaard JF (1995) Wave-guides formed by multiple layers of dielectric, semiconductor, or metallic media with optical loss and anisotropy. J Opt Soc Am A 12(10):2122–2128
12. Mendes SB, Bradshaw JT et al (2004) Technique for determining the angular orientation of molecules bound to the surface of an arbitrary planar optical waveguide. Appl Opt 43(1):70–78
13. Zannoni C, Arcioni A et al (1983) Fluorescence depolarization in liquid-crystals and membrane bilayers. Chem Phys Lipids 32(3–4):179–250
14. Runge AF, Saavedra SS et al (2006) Combination of polarized TIRF and ATR spectroscopies for determination of the second and fourth order parameters of molecular orientation in thin films and construction of an orientation distribution based on the maximum entropy method. J Phys Chem B 110(13):6721–6731
15. Kremeskötter J, Wilson R et al (1995) Detection of glucose via electrochemiluminescence in a thin-layer cell with a planar optical waveguide. Meas Sci Technol 6:1325–1328
16. Tien PK, Ulrich R (1970) Theory of prism-film coupler and thin-film light guides. J Opt Soc Am 60(10):1325–1337
17. Kato K, Takatsu A et al (1995) A slab-optical-wave-guide absorption-spectroscopy of Langmuir-Blodgett-films with a white-light excitation source. Chem Lett 6:437–438
18. Bradshaw JT, Mendes SB et al (2002) A simplified broadband coupling approach applied to chemically robust sol-gel, planar integrated optical waveguides. Anal Chem 74(8):1751–1759
19. Mendes SB, Li LF et al (1997) Achromatic prism-coupler for planar waveguide. Opt Commun 136(3–4):320–326
20. Dakss ML, Kuhn L et al (1970) Grating coupler for efficient excitation of optical guided waves in thin films. Appl Phys Lett 16(12):523–525
21. Harris JH, Winn RK et al (1972) Theory and design of periodic couplers. Appl Opt 11 (10):2234–2241
22. Kogelnik H, Sosnowski TP (1970) Holographic thin film couplers. Bell Syst Tech J 49(7):1602–1608
23. Li L, Xu M et al (1987) Fabrication of photoresist masks for submicrometer surface relief gratings. Proc SPIE 835:72–82
24. Tamir T (1982) Integrated optics. Springer, Berlin
25. Mendes SB, Li LF et al (1995) 70-nm-bandwidth achromatic wave-guide coupler. Appl Opt 34(27):6180–6186
26. Mendes SB, Li LF et al (1996) Broad-band attenuated total reflection spectroscopy of a hydrated protein film on a single mode planar waveguide. Langmuir 12(14):3374–3376
27. Itoh K, Fujishima A (1988) An application of optical waveguides to electrochemistry: construction of optical waveguide electrodes. J Phys Chem 92:7043–7045

28. Itoh K, Fujishima A (1992) An application of optical waveguides to electrochemical and photoelectrochemical processes. In: Murphy OJ, Srinivasan S, Conway BE (eds) Electrochemistry in transition. Plenum, New York, pp 219–225
29. Piraud C, Mwarania E et al (1992) An optoelectrochemical thin-film chlorine sensor employing evanescent fields on planar optical waveguides. Anal Chem 64:651–655
30. Piraud C, Mwarania EK et al (1992) Optoelectrochemical transduction on planar optical wave-guides. J Lightwave Technol 10(5):693–699
31. Bard AJ, Faulkner LR (1980) Electrochemical methods. Wiley, New York
32. Bowden EF (1997) Wiring mother nature: interfacial electrochemistry of proteins. Electrochem Soc Interface 6:40–44
33. Gorton L, Lindgren A et al (1999) Direct electron transfer between heme-containing enzymes and electrodes as basis for third generation biosensors. Anal Chim Acta 400:91–108
34. Hawkridge FM, Taniguchi I (1995) The direct electron transfer reactions of cytochrome c at electrode surfaces. Comments Inorg Chem 17:163–187
35. Song S, Clark RA et al (1993) Characterization of cytochrome c/alkanethiolate structures prepared by self-assembly on gold. J Phys Chem 97:6564–6572
36. Robertson RT (2002) The development of electroactive total internal reflection optical devices for the characterization of metalloprotein films. PhD dissertation. Department of Chemistry, Tucson, Arizona
37. Ross SE, Seliskar CJ et al (2000) Spectroelectrochemical sensing based on multimode selectivity simultaneously achievable in a single device. 9. Incorporation of planar waveguide technology. Anal Chem 72:5549–5555